Monthly Notices
of the
ROYAL ASTRONOMICAL SOCIETY

MNRAS **429,** 75–84 (2013) doi:10.1093/mnras/sts320

Ultraviolet and X-ray variability of NGC 4051 over 45 days with *XMM–Newton* and *Swift*

W. N. Alston,[1]⋆ S. Vaughan[1] and P. Uttley[2]

[1]*X-Ray and Observational Astronomy Group, University of Leicester, Leicester LE1 7RH*
[2]*Astronomical Institute Anton Pannekoek, University of Amsterdam, Postbus 94249, NL-1090 GE Amsterdam, the Netherlands*

Accepted 2012 October 29. Received 2012 October 24; in original form 2012 October 9

ABSTRACT

We analyse 15 *XMM–Newton* observations of the Seyfert galaxy NGC 4051 obtained over 45 d to determine the ultraviolet (UV) light curve variability characteristics and search for correlated UV/X-ray emission. The UV light curve shows variability on all time-scales, however with lower fractional rms than the 0.2–10 keV X-rays. On days–weeks time-scales the fractional variability of the UV is $F_{\rm var} \sim 8$ per cent, and on short ($\sim$ hours) time-scales $F_{\rm var} \sim 2$ per cent. The *within-observation* excess variance in 4 of the 15 UV observations was found to be much higher than the remaining 11. This was caused by large systematic uncertainties in the count rate masking the intrinsic source variance. For the four 'good' observations we fit an unbroken power-law model to the UV power spectra with slope -2.6 ± 0.5. We compute the UV/X-ray cross-correlation function for the 'good' observations and find a correlation of $\sim$0.5 at a time lag of $\sim$3 ks, where the UV lags the X-rays. We also compute for the first time the UV/X-ray cross-spectrum in the range 0–28.5 ks and find a low coherence and an average time lag of $\sim$3 ks. Combining the 15 *XMM–Newton* and the *Swift* observations we compute the discrete correlation function over $\pm$40 d but are unable to recover a significant correlation. The magnitude and direction of the lag estimate from the four 'good' observations indicate a scenario where $\sim$25 per cent of the UV variance is caused by thermal reprocessing of the incident X-ray emission.

Key words: galaxies: active – galaxies: Seyfert – ultraviolet: galaxies – X-rays: galaxies.

1 INTRODUCTION

The broad-band spectral energy distribution (SED) of active galactic nuclei (AGN) requires multiple emission components, including thermal and non-thermal mechanisms (Shang et al. 2011). The energy output in Seyfert galaxies and quasars is dominated by the ultraviolet (UV) emission, thought to be mostly thermal emission from the inner parts of an accretion disc surrounding the central supermassive black hole (SMBH). The location of the UV emitting region depends on the details of the accretion flow, and these in turn depend on the black hole mass and accretion rate, but is typically $\sim$10–1000$r_{\rm g}$ (where $r_{\rm g} = GM_{\rm BH}/c^2$ is the gravitational radius). By contrast the X-ray spectrum is usually interpreted as the result of inverse-Compton scattering of soft thermal photons by an optically thin corona of hot electrons in the central few tens of $r_{\rm g}$ from the black hole (e.g. Haardt & Maraschi 1991).

The causal connections between these processes are still unclear but can in principle be investigated by studying the time variations in the luminosity across different wavebands. Strong UV and X-ray variability is common to AGN on a wide range of time-scales (e.g. Collin 2001), with the most rapid variations seen in X-rays (e.g. Mushotzky, Done & Pounds 1993). If the emission mechanisms are coupled the UV and X-ray variations should be correlated, in which case the direction and magnitude of time delays should reveal the causal relationship. Two favoured coupling mechanisms are (i) Compton up-scattering of UV photons – produced in the disc – to X-ray energies in the corona (Haardt & Maraschi 1991), and (ii) thermal reprocessing in the disc of X-ray photons produced in the corona (Guilbert & Rees 1988). The interaction time-scale for these two processes is approximately the light crossing time between the two emitting regions, and will be in the region of minutes to days for black hole masses $M_{\rm BH} \sim 10^6$–10^8 M$_\odot$.

Both emission regions are also likely to be correlated at some level if they are both modulated by their local accretion rate, which varies as accretion rate fluctuations propagate through the flow (e.g. Arévalo & Uttley 2006). In a standard accretion disc the time-scale for propagation of fluctuations between the two emission regions is governed by the viscous time-scale of the disc. For $M_{\rm BH} \sim 10^6$–10^8 M$_\odot$ this time-scale will be in the region of weeks

⋆ E-mail: wna3@leicester.ac.uk

to years (Czerny 2006). If any of these processes are significant, their effects should be apparent from time series analysis of light curves from both wavebands. A combination of these processes occurring at the same time could make individual reprocessing models harder to detect.

Studies of correlations between variations in different wavebands are a potentially powerful tool for investigating the connections between different emission mechanisms (see Uttley 2006 for a short review). X-ray/optical correlations on long time-scales have been seen in radio-quiet AGN (e.g. Uttley et al. 2003; Arévalo et al. 2008, 2009; Breedt et al. 2009). Together with the optical–optical lags (e.g. Cackett, Horne & Winkler 2007) they imply that a combination of accretion fluctuations and reprocessing produces much of the optical variability. X-ray/UV correlations have been seen in e.g. Nandra et al. (1998) and Cameron et al. (2012); however, there are currently fewer examples than the X-ray/optical correlation studies.

The target of the present paper – the low-mass Narrow line Seyfert 1 (NLS1) galaxy NGC 4051 – has been the subject of several such studies. Done et al. (1990) obtained ∼3 d of contemporaneous X-ray, UV, optical and IR data, but found little variability at longer wavelengths despite strong, rapid X-ray variations. Using light curves spanning ∼1000 d in the optical and X-rays, Peterson et al. (2000) revealed significant optical variability on longer time-scales that appeared to be correlated with the (longer time-scale) X-ray variations. Shemmer et al. (2003) and Breedt et al. (2010) also found a significant X-ray/optical correlation, the latter using ∼5000 d of monitoring data. On shorter time-scales, Mason et al. (2002) and Smith & Vaughan (2007) used ∼2 d *XMM–Newton* observations to search for X-ray/UV correlations, with inconclusive results.

The rest of this paper is organized as follows. Section 2 discusses the observations of NGC 4051 and extraction of the X-ray and UV light curves. Section 3 gives an analysis of the variability amplitudes and UV power spectral density (PSD), cross-correlations are discussed in Section 4 and the implications of these results are discussed in Section 5.

2 OBSERVATIONS AND DATA REDUCTION

2.1 Target and observations

NGC 4051 is a nearby ($z = 0.0023$) NLS1 galaxy with black hole mass $M_{\rm BH} \approx 1.7 \pm 0.5 \times 10^6\,{\rm M}_\odot$ (Denney, Watson & Peterson 2009) at a Tully–Fisher distance, $D \approx 15.2$ Mpc (Russell 2002).

Simultaneous, or quasi-simultaneous, observations of the two bands are required in order to search for correlated variability. The *XMM–Newton* and *Swift* observatories are suited for this task. The three European Photon Imaging Camera (EPIC) X-ray detectors (pn; Strüder et al. 2001, MOS1/2; Turner et al. 2001) and co-aligned Optical Monitor (OM; Mason et al. 2001) make *XMM–Newton* an ideal instrument for probing the X-ray to UV correlation on short time-scales. The rapid response and flexible scheduling of *Swift* (Gehrels et al. 2004), with the X-ray Telescope (XRT; Burrows & The Swift XRT Team 2004) and co-aligned Ultraviolet/Optical Telescope (UVOT; Roming, Kennedy & Mason 2005), allow for X-ray and UV monitoring on longer time-scales.

NGC 4051 was observed by *XMM–Newton* in 15 separate observations over a period of 45 d during 2009 May–June. Each observation lasted ∼40 ks giving a total of ∼580 ks of usable data. Individual observation details are listed in Table 1. We make use of the EPIC-pn detector in small window mode, with an ∼4 × 4 arcmin field of view. With roughly the same start and end time as the OM, this gives a total of ∼530 ks of simultaneous UV and X-ray data.

Table 1. *XMM–Newton* observation summary. The columns list (1) the spacecraft revolution number, (2) the start date of the observation, (3) the EPIC-pn observation duration, (4) the OM observation duration and (5) the number of OM images in each observation.

XMM rev. no.	Observation Date (Y-M-D)	EPIC-pn On time (s)	OM On time (s)	No. OM images
1721	2009-05-03	45 717	45 105	33
1722	2009-05-05	45 645	45 103	33
1724	2009-05-09	45 548	45 003	33
1725	2009-05-11	45 447	44 903	33
1727	2009-05-15	32 644	31 340	21
1728	2009-05-17	42 433	37 367	26
1729	2009-05-19	41 813	41 267	26
1730	2009-05-21	41 936	40 894	26
1733	2009-05-27	44 919	39 168	22
1734	2009-05-29	43 726	43 182	27
1736	2009-06-02	44 946	44 164	22
1737	2009-06-04	39 756	34 574	23
1739	2009-06-08	43 545	43 000	27
1740	2009-06-10	44 453	43 909	28
1743	2009-06-16	42 717	42 116	26

All of the OM observations were taken in *Imaging Mode* in the UVW1 filter (central wavelength 2910 Å) with 2 × 2 pixel binning. This gives a field of view of 8 × 8 arcmin and a spatial resolution of 0.95 arcsec pixel^{-1}. The exposure length varied between 1000 and 1400 s from observation to observation, giving ∼30 exposures per observation and a total of 406 across all 15 observations.

To complement the *XMM–Newton* data set, 51 *Swift* Target of Opportunity (ToO) observations were made covering the same epoch. The observations are separated by ∼1 d and typically ∼1.5 ks long, with 1–3 UVOT exposures per observation, giving a total of 71 frames. The UVOT exposures were taken in the $uvw1$ filter, which has approximately the same bandpass as the OM UVW1, with a field of view of 17 × 17 arcmin and a pixel scale of 0.5 arcsec. The XRT has a 23 × 23 arcmin field of view with a pixel scale of 0.236 arcsec and covers the energy range 0.2–10.0 keV, similar to EPIC-pn.

2.2 OM light curves

The Observation Data Files (ODFs) for our target were extracted from the *XMM–Newton* Science Archive (XSA) and processed using the *XMM–Newton* Science Analysis System (SAS, v11.0.0) routine OMICHAIN. Custom-made IDL[1] scripts were made to perform source photometry and apply instrumental corrections. Source counts were extracted in a 6 arcsec radius aperture for the galaxy nucleus and three field stars present in the images. Background counts were extracted in a 30 arcsec radius aperture, placed in a region away from the host galaxy and field stars. Accurate count rates from aperture photometry of the OM images can only be produced once five instrumental corrections have been applied (Mason et al. 2001). These are, in order of application to the extracted counts, the point spread function (PSF1), coincidence loss (CL), CCD dead-

[1] http://www.exelisvis.com

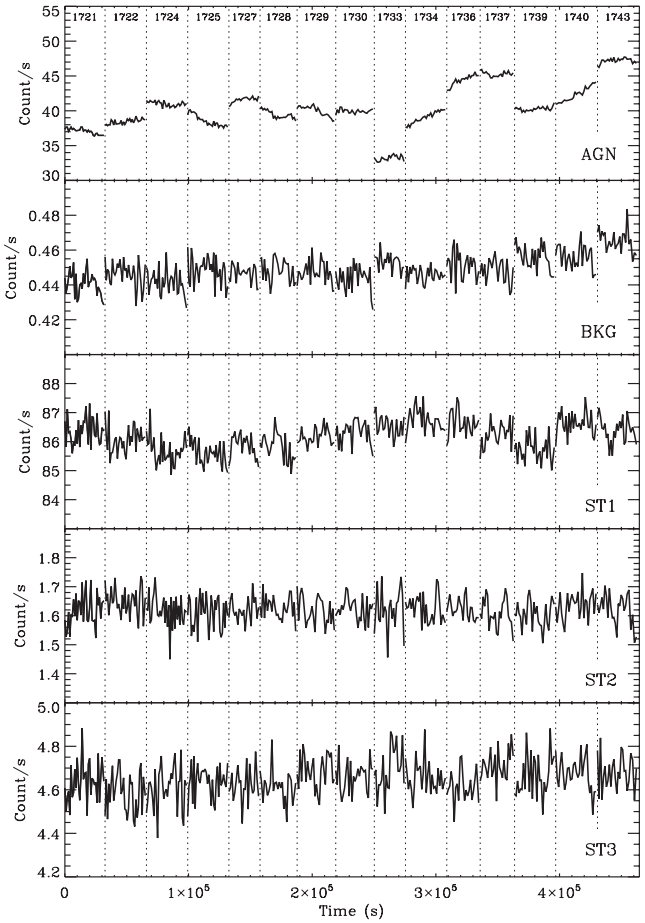

Figure 1. Concatenated light curves for the *XMM* OM sources. From the top to the bottom panel they are central nucleus, background region and field stars 1, 2 and 3, respectively.

time (DT), the UV point spread function (PSF2) and time-dependent sensitivity degradation (TDS) corrections. The concatenated background subtracted light curves for the *XMM* OM sources and background region are shown in Fig. 1.

In the UVW1 filter there will be a significant contribution to the observed nuclear light from the host galaxy. This should be constant (to within the random and systematic errors of the aperture photometry) and so we have not tried to remove it, but as such it should not affect the PSD or correlation analysis in any important way.

As a test of the background subtraction and photometry procedure we tested for (zero lag) correlations between the background subtracted light curves of the sources and a second background region for all 15 observations. For ∼400 data points a Pearson linear correlation coefficient $r \geq 0.13$ indicates a weak but statistically significant correlation ($p < 0.01$). We find no significant correlation between each of the background subtracted sources, but in the source versus background tests, values of r up to 0.3 are observed. The strength of this correlation is also observed to change between 0.0 and 0.3 when using a different background region. The mean correlation coefficient between source versus source and source versus background for individual observations is very low ($-0.1 \lesssim r \lesssim 0.1$). This indicates that the correlation is caused by changes in the background over the course of the 15 observations. We are cautious of this fact during the rest of the analysis and use source light curves subtracted using various background regions. We find that the choice of background region has no effect on any subsequent analysis.

2.3 EPIC-pn light curves and spectra

The EPIC-pn light curves used in this analysis are the same as those used in Vaughan et al. (2011). The raw EPIC-pn data were processed from the ODFs using the SAS (v11.0.0). Events lists were filtered using PATTERN 0–4, FLAG = 0 and were visually inspected for background flaring. Light curves were extracted from the filtered events files using a source aperture of radius 35 arcsec and a non-overlapping larger background region on the same chip. Light curves were extracted with a bin size of $\Delta t = 5$ s and an energy range of 0.2–10.0 keV. The background subtracted EPIC-pn light curves are shown in the bottom panel of Fig. 2. Spectra were extracted and binned to a minimum of 25 counts per bin. Response files were created using RMFGEN v1.55.2 and AFRGEN v.1.77.4.

2.4 UVOT and XRT light curves

Visual inspection of the 71 UVOT exposures revealed considerable target movement in 40, leaving 31 usable frames. The exposure time varied slightly across the observations but is typically ∼500 s. The HEASOFT (v6.10) task UVOTSOURCE was used to extract source counts from the galaxy nucleus and the same field stars used in the OM photometry. The optimum extraction radius is 12.5 pixels (∼6 arcsec) for the $uvw1$ filter (Poole et al. 2008). A 60 pixel radius background aperture fixed in sky coordinates in a blank region of the sky was also extracted. Similar to the OM, instrumental corrections – PSF1, CL, DT, PSF2 and TDS – must be applied to the counts extracted in each aperture on the UVOT images. UVOTSOURCE automatically performs background subtraction and applies these corrections based on the most up-to-date instrument calibration data base (CALDB 4.1.2). The background subtracted UVOT light curves are shown in the lower panel of Fig. 2. We extract XRT counts in the 0.2–10 keV range using the online XRT Products Builder (Evans, Beardmore & Page 2009). This performs all the necessary processing and provides background subtracted light curves.

3 DATA ANALYSIS

3.1 Quantifying variability

In an observed light curve some of the total variance will be intrinsic to the source and some will come from variations in the measurement uncertainties (Vaughan et al. 2003). The difference between the two is the 'excess variance', and can be used to estimate the intrinsic source variance. The values of the variability estimators for the OM and UVOT sources are listed in Table 2. The variability statistics calculated over the whole ∼45 d *XMM–Newton* observation show that there is significant variability in NGC 4051, with $F_{\rm var} \approx 8$ per cent. On time-scales within each observation, the variability is weaker than on long time-scales.

In 11 of the *XMM–Newton* observations the excess variance in the nucleus and star 1 values are almost identical. This indicates that there is a 'floor' in the excess variance, which is not accounted for by the errors. We refer to this as a systematic error but are unable to account for it. In the 11 observations this systematic error is too large to detect any intrinsic variability from the nucleus. The variability estimators in Table 2 show that the nucleus in the remaining four 'good' observations clearly possesses significant variability compared to the field stars, and as such will be treated

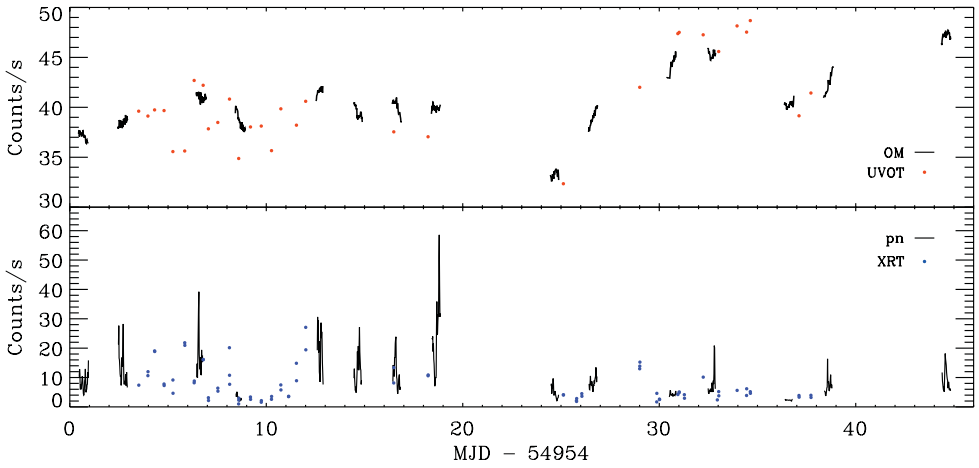

Figure 2. Between-observation variability for UV (top) and X-ray (bottom) from *XMM* and *Swift*. In the top panel the black lines are the OM data and the red circles are the UVOT. In the bottom panel the black lines are the EPIC-pn data and the blue dots the XRT. In both panels the *Swift* count rates have been scaled up to account for different effective areas (see Section 4.2 for details).

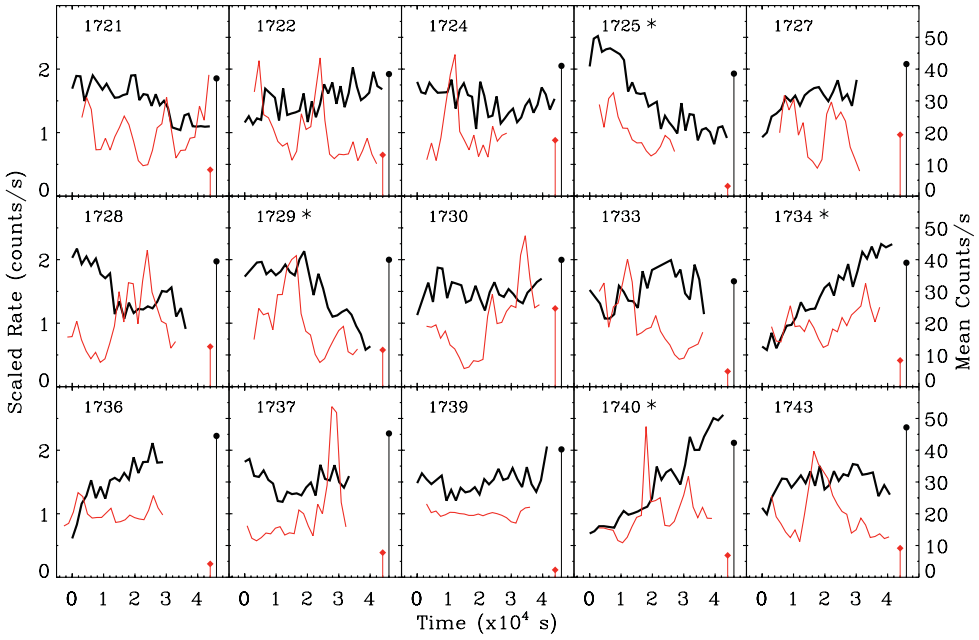

Figure 3. Within-observation X-ray and UV variability from the 15 *XMM–Newton* observations. To better represent the light curves the OM (thick black) has been scaled to some arbitrary value and shifted to a mean of 1.5 ct s^{-1}. The EPIC-pn (thin red) has been normalized to a mean rate of 1 ct s^{-1}. The circle and diamond markers represent the mean observation count rate, given by the right ordinate, for the OM and EPIC-pn, respectively. The four 'good' OM observations are indicated by the asterisks next to the revolution number.

separately from the 11 'poor' observations in the correlation analysis in Section 4. The 'good' UV observations are revolutions 1725, 1729, 1734 and 1740, and are indicated by an asterisk in Fig. 3.

3.2 The UV power spectrum

The PSD describes the amount of variability power present in the light curve (mean squared amplitude) as a function of temporal frequency. The PSD of the X-ray light curves is discussed by Vaughan et al. (2011). The UV power spectrum was estimated from the 15 individual OM observations using standard methods (e.g. van der Klis 1989). A 30 ks segment (equal to the shortest observation length) was taken from each observation. Within each *XMM–Newton* observation the individual OM exposures are approximately evenly sampled in time, although the exposure times do differ between observations (from 1200 to 1500 s). The basic periodogram requires evenly sampled data, and so we interpolated all OM data on to a grid evenly sampled at $\Delta t = 1500$ s – the smoothness of the OM light curves means that linear interpolation should not affect the shape of the time series in any significant manner. The observed power spectrum may be distorted by leakage of power from low frequencies to higher frequencies (van der Klis 1989; Uttley, McHardy & Papadakis 2002; Vaughan et al. 2003). This can bias the data such that the observed spectrum resembles an $\alpha = 2$ power law even if the true power spectrum is somewhat steeper.

Fig. 4 shows the power spectrum for the NGC 4051 nucleus, star 1, star 3 and the background for the 15 *XMM–Newton* OM observations. Periodograms were computed with absolute

Table 2. Quantifying source UV variability. The columns give the following information: (1) source name, (2) mean count rate, (3) sample standard deviation, (4) excess variance, (5) fractional, excess rms amplitude ($F_{\rm var}$). The upper table shows the values obtained by combining all 15 *XMM–Newton* OM observations. The second and third tables show the values obtained by averaging the results from each of the 4 'good' and 11 'poor' *XMM–Newton* OM observations, respectively. The lower table shows the results from the *Swift* UVOT observations.

Object	Mean rate (ct s^{-1})	σ (ct s^{-1})	$\sigma^2_{\rm XS}$ (ct s^{-2})	$F_{\rm var}$ (per cent)
	XMM–Newton total			
Nucleus	40.5	3.19	10.1	7.9
Star 1	86.2	0.55	0.24	0.6
Star 2	1.6	0.05	0.0005	1.5
Star 3	4.6	0.09	0.003	1.2
Background	0.4	0.14	0.015	2.6
	XMM–Newton 'good' 4 observation averages			
Nucleus	40.0	0.84	0.69	2.1
Star 1	86.3	0.37	0.09	0.3
Star 2	1.6	0.05	0.0005	0.2
Star 3	4.7	0.08	0.001	0.6
Background	0.4	0.006	0.005	1.0
	XMM–Newton 'poor' 11 observation averages			
Nucleus	40.7	0.40	0.14	0.9
Star 1	86.2	0.42	0.13	0.4
Star 2	1.6	0.05	0.0004	0.1
Star 3	4.6	0.08	0.003	0.9
Background	0.4	0.007	0.007	1.8
	Swift total			
Nucleus	40.1	4.39	19.2	10.8
Star 1	48.5	1.06	1.01	0.02
Star 2	1.1	0.04	−0.001	0.02
Star 3	3.1	0.09	0.002	0.01

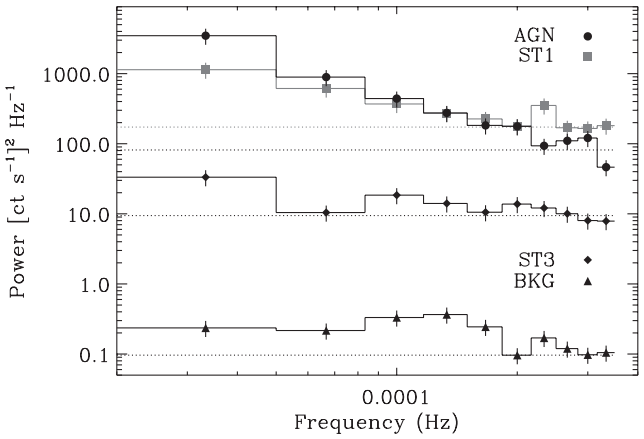

Figure 4. UV power spectrum in absolute units for the background subtracted OM sources, produced from the 15 *XMM* observations. The circles, squares and diamonds represent NGC 4051, star 1 and star 3, respectively. The triangles are the power spectrum estimate for the background light curves subtracted by a background region on the opposite side of the CCD, see the text for details. The dotted lines are the Poisson noise estimates for each source.

normalization and the Poisson noise level is estimated using the formula in Vaughan et al. (2003, appendix A). The background power spectrum is computed for the light curve from the background region (the same background region used in the source background subtraction) subtracted by a second background region

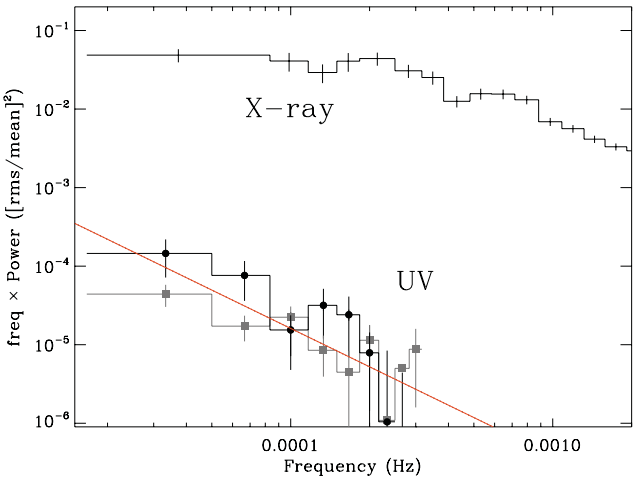

Figure 5. UV power spectrum produced from the *XMM* OM observations. The black circles are the average of the 4 'good' periodograms and the grey squares are the average of the 11 'poor' periodograms, prior to subtraction of Poisson noise. The red solid line is the power-law fit to the 'good' data. The upper solid black line is the Poisson noise subtracted X-ray (0.2–10 keV) power spectrum from Vaughan et al. (2011).

on the opposite side of the CCD. In all sources, some power above the noise level is present. This is most likely the result of the background subtraction issues described in Section 2.2. Star 1 shows a similar red-noise slope, albeit with less power, to the nucleus. A cross-correlation test (see Section 4) between the nucleus and star 1 revealed no significant correlation between the two sources. This indicates that the variations in star 1 are either intrinsic to the star or caused by the problems in the background subtraction.

Fig. 5 shows the resulting NGC 4051 power spectrum from the 'good' and 'poor' OM data, and a two-component model is fit to the 'good' data. Periodograms were computed with fractional rms normalization (Vaughan et al. 2003, appendix A). We did not subtract the expected contribution from Poisson noise but instead included this in the model fitting. The simple model comprises a power law plus constant to account for the Poisson fluctuations in the count rate: $P(\nu) = A\nu^{-\alpha} + P_N$ (where ν is the temporal frequency, A is a normalization term, α is the power-law index and P_N is the power density due to Poisson noise). This was fitted to the data using XSPEC v12.6.0 (Arnaud 1996). The P_N level was allowed to vary freely. Using a χ^2 statistic the best fit to the data is found to have $\alpha = 2.62 \pm 0.48$ and $P_N = 0.059 \pm 0.023$, with $\chi^2 = 3.7$ for seven degrees of freedom (7dof). The Poisson noise level can also be estimated from the formula given in Vaughan et al. (2003) which we compute to be $P_N = 0.05$, in agreement with the value derived from the PSD. As expected, fitting the model assuming a fixed $P_N = 0.05$ value gave consistent results for the index parameter ($\alpha = 2.50 \pm 0.35$), with $\chi^2 = 3.9$ for 8dof. Errors on the model parameters correspond to a 90 per cent confidence level for each interesting parameter (i.e. a $\Delta\chi^2 = 2.7$ criterion). For comparison, the X-ray PSD from Vaughan et al. (2011) is plotted in Fig. 5.

4 CORRELATION ANALYSIS

In this section we discuss tests for X-ray/UV correlations on short time-scales within each observation (*within-observations*) and longer time-scale (*between-observations*). Treated individually, each of the 15 *XMM* observations allowed us to probe time-scales

of ∼ 2–40 ks. Combining the *XMM* and *Swift* light curves allowed us to look for any long-term trends in correlation between the two bands over the ∼45 d.

4.1 Within-observation correlations

Standard time series analysis methods (cf. Box & Jenkins 1976; Priestley 1981) require the two light curves to be simultaneous and evenly sampled. This requirement is complicated by the OM and EPIC-pn not always starting and ending at the same time, the irregular sampling of the OM, the read-out time of the OM CCD and any bad OM exposures. Where the two light curves are simultaneous we linearly interpolate the OM on to a uniformly sampled regular grid. Given that the OM light curves vary smoothly within each observation, linear interpolation should not have a significant effect on the intrinsic variability. The EPIC-pn X-ray counts are re-binned to be contiguous and simultaneous with the OM bins by taking the average count rate within the new bin width. We chose a bin width of 1500 s to be consistent with the mean sampling rate of the OM (1502 s) across the 15 *XMM* observations. The simultaneous light curve lengths range from 28.5 to 43.5 ks.

4.1.1 The correlation function

The cross-correlation function (CCF) is a standard tool for measuring the degree of correlation between two evenly sampled time series (x_t, y_t) as a function of time lag (cf. Box & Jenkins 1976; Priestley 1981). We estimated the CCF for each *XMM–Newton* observation individually using the IDL function C_CORRELATE, shown in panel (a) of Fig. 6, where a positive lag in the plot indicates that the UV variations are lagging those of the X-rays. A large spread in the CCF value for any computed time lag is seen. Panel (b) of Fig. 6 shows the average CCF for all 15 *XMM* observations. The strongest feature is the peak in the CCF around ∼4.5 ks, although with a correlation of ∼0.1, which falls within the confidence intervals. Confidence intervals on the average CCF are estimated using Monte Carlo simulations, where the 95 and 99 per cent confidence intervals are shown in Fig. 6. These show the expected range of CCF values under the assumption that the X-ray and UV processes are independent, i.e. in the absence of a real correlation. The full details of these simulations are given in Appendix A. The error on the average CCF is given by the standard error for N observations at each time lag t.

Panel (c) in Fig. 6 shows the average CCF plot for the four 'good' observations (see Section 3). A distinct broad peak can be seen around ∼3 ks with a correlation of ∼0.5, which lies outside the 99 per cent confidence interval. Confidence intervals are calculated in the same way as above except that four simulated light curves are averaged over in each CCF estimate. The small error bars on the averaged 'good' CCF shows that there is little scatter in the individual CCF measurements.

A correlation between optical light curves and X-ray photon index has been detected in some sources (e.g. Nandra et al. 2000), despite there being a weak correlation between the optical and X-ray light curves. We therefore cross-correlated the UV light curves with the 0.7–2/2–10 keV hardness ratio (a proxy for photon index) but find a CCF shape similar to that between the UV and X-ray light curves. This is most likely due to the X-ray spectral shape changes being strongly correlated with the overall X-ray flux.

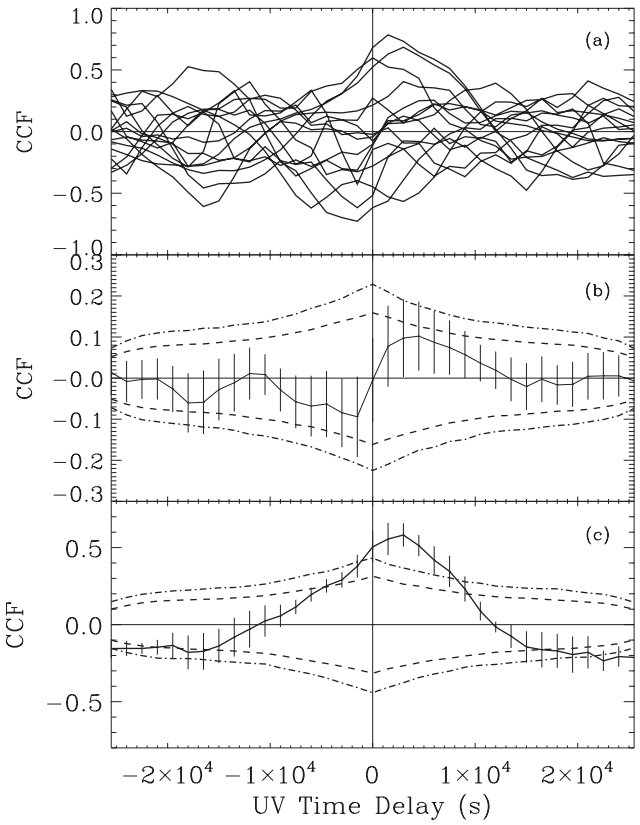

Figure 6. The CCF for the 15 *XMM* observations. The top panel is the individual CCF for each observation, the middle panel is the average CCF of all 15 observations, whilst the bottom panel is the average CCF for the 4 'good' observations. The dashed and dot–dashed lines are the 95 and 99 per cent confidence intervals, respectively, calculated individually for each data subset. Confidence intervals were estimated using Monte Carlo simulations of light curves assuming no correlation (see Appendix A).

4.1.2 The cross-spectrum

The cross-spectrum is the Fourier transform of the CCF (Box & Jenkins 1976; Priestley 1981), and has been widely used in analysing X-ray light curves from X-ray binaries (e.g. Miyamoto & Kitamoto 1989; Vaughan & Nowak 1997; Nowak et al. 1999) and more recently from AGN (e.g. Fabian et al. 2009). It contains the same information as the CCF but represents the time lags and strength of correlation in terms of phase difference and coherence as a function of temporal (Fourier) frequency. The phase lag $\Delta\phi$ can be expressed as a time lag at a given frequency ν: $\tau = \Delta\phi/2\pi\nu$. Under quite general conditions the phase delay estimates are approximately independent at each frequency; by contrast, adjacent values of the CCF tend to be correlated due to the autocorrelation of the individual time series. Here we have estimated the cross spectrum using the 'good' OM data, except that the segments have been trimmed to equal length (28.5 ks), corresponding to the shortest simultaneous light curve. The resulting coherence and phase parts of the cross-spectrum are shown in Fig. 7. Errors were estimated using standard formulae (Vaughan & Nowak 1997), and confidence intervals were estimated using simulated light curves (see Appendix A for details).

The coherence between the two bands is found to be low ($\leq$0.2) at all frequencies. The average time lag of the lowest five frequency bins is ∼3 ks, consistent with what is seen in the CCF. A low

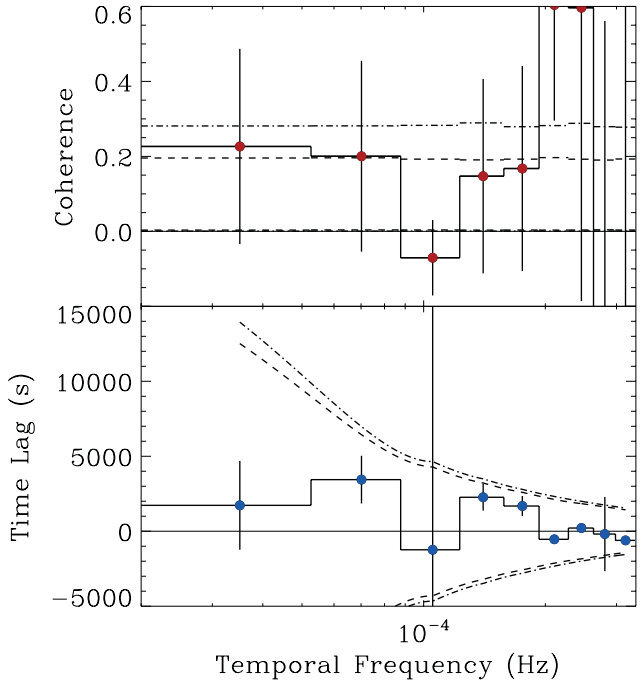

Figure 7. The coherence and phase-lag parts of the cross-spectrum for the combined four 'good' *XMM* observations. The dashed and dot–dashed lines are the 95 and 99 per cent confidence intervals, respectively. Confidence intervals were estimated using Monte Carlo simulations of light curves assuming no correlation (see Appendix A).

coherence means that the errors on the time delay estimates are most likely underestimated using standard formulae, which can increase the apparent significance of lags when the errors are estimated using the standard formula and the intrinsic coherence is very low (e.g. Bendat & Piersol 1986). The cross spectrum is also computed for the combined 15 *XMM* observations which gives a coherence consistent with zero for each frequency bin, and the average time lag in the lowest five bins is consistent with that found with the four 'good' observations.

4.1.3 Pre-processing the light curves

The OM light curves tend to be dominated by slow, quasi-linear trends, and these can affect the CCF estimation (Welsh 1999). We have repeated the CCF and cross-spectrum analysis after 'end-matching' the OM light curves (i.e. removing a linear trend such that the first and last points are level – see Fougere 1985). This 'end-matching' removes, to a large extent, linear trends from the data and alleviates the problem caused by circularity of the Fourier transform when estimating the cross spectrum.

We end-matched the *XMM* OM light curves individually and computed the CCF and cross-spectrum using the same X-ray light curves as before. The CCF for both the 'good' and *all* the data remains mostly unchanged. In the cross-spectrum the phase lag follows the same distribution and the coherence remains low in both cases. As this reanalysis did not substantially alter the results we do not show the CCF and cross-spectrum plots here.

4.2 Between-observation correlations

Given the extended period and sampling of the *XMM* and *Swift* observations, we are able to search for possible correlations and time lags on longer time-scales. The *XMM–Newton* data (EPIC-pn and OM) and *Swift* data (XRT and UVOT) were first treated separately and then combined to produce one X-ray and one UV light curve. In either case the time sampling between observations is highly uneven, and so the discrete correlation function (DCF; Edelson & Krolik 1988) was used to estimate the CCF. We use all the *XMM–Newton* OM data in this part of the analysis, as the variations within each OM observation will have little effect on the DCF.

For the *XMM* data set, the midpoint of each original OM exposure was used. The EPIC-pn data were binned to be contiguous from the start of each revolution, with a bin size of 1500 s to be consistent with the mean OM sampling rate. A 10 ks DCF bin width is adopted to be consistent with the mean OM sampling rate over the extended observation. Although the OM exposure length varied between 1200 and 1500 s from revolution to revolution, we treat the source count rate in each exposure as a representative of the average count rate. As the source varies smoothly in the UVW1 filter we do not expect this to have any effect on the shape of the DCF. We test this by computing the DCF using the OM data that were binned on to a 1500 s even grid, and find no change in the shape of the DCF. The DCF for the *XMM* data set for the range $-40 < \mathrm{lag} < +40$ d is shown in Fig. 8, where a positive lag means the UV are lagging the X-rays. Some peaks can be seen in the DCF but all lie within the confidence intervals. The peaks are most likely the result of the DCF binning used, combined with the underlying shape of the uncorrelated red-noise light curves.

For the *Swift* data set, the UVOT exposures from each snapshot were used to represent the mean source count rate in the middle of each exposure bin. Again the exposure lengths varied from ∼300 to 800 s with a mean of ∼500 s, but due to the steepness of the red-noise power spectrum this will have no effect on the shape of the DCF

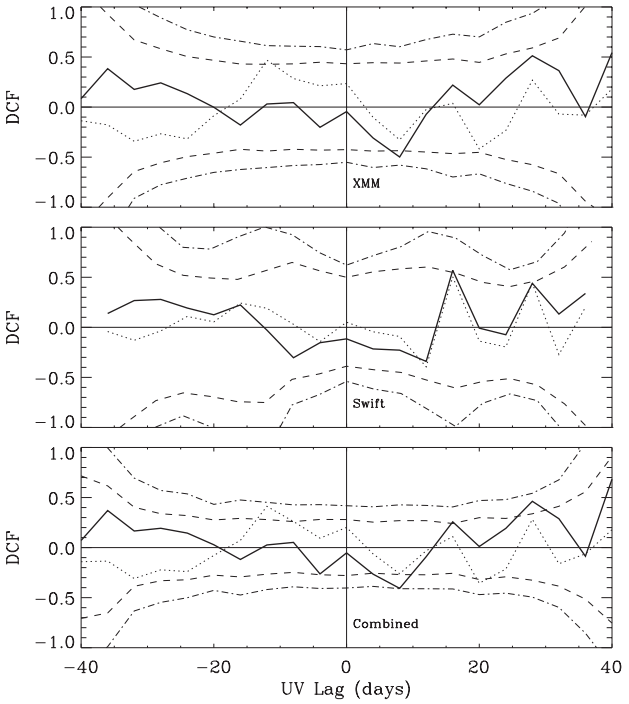

Figure 8. The DCF for the between-observations (solid black line). The dotted black line is the DCF for the end-matched data. The dashed and dot–dashed lines represent the 90 and 95 per cent confidence intervals, respectively.

as long as the DCF bin size is much greater than the mean UVOT exposure length. The XRT counts are taken from each snapshot and have a mean exposure length of ∼500 s. The DCF for the *Swift* data is plotted in Fig. 8. The plotted 95 and 99 per cent confidence intervals are calculated using simulated light curves following the method outlined in Appendix A.

To make the most of the observational coverage we combine the *XMM* and *Swift* data sets and recompute the DCF. As the effective areas of the UV and X-ray instruments on either telescope are not identical the count rates from one telescope need to be scaled before the DCF can be computed. We estimate this scale factor using the three occasions the observations overlap and find OM ≈ 1.1 × UVOT, and EPIC-pn ≈ 15 × XRT. The scaling factor for the X-ray cameras is consistent with that calculated by WEBPIMMS.[2] No reference for a scaling factor between the UV cameras could be found, but we find that the choice of the scaling factor within the range ∼0.5–1.5 has no effect on the shape of the DCF.

In Fig. 2 it can be seen that the UV light curves show a gradual increase in counts over the extended observation. To account for any underlying long-term trends in the UV variability we 'end-match' the overall UV light curve and recompute the DCF for the individual and combined data sets. These are shown as the dotted black lines in Fig. 8.

5 DISCUSSION

Using UV and X-ray data from *XMM–Newton* and *Swift* we have analysed the light curves of NLS1 galaxy NGC 4051 to search for correlations in the variability between the two bands. UV variability is detected on short and long time-scales; however, the fractional rms amplitude is smaller than that in the X-rays. On days–weeks time-scales the fractional variability of the UV is $F_{\rm var} \sim 8$ per cent, and on short (∼hours) time-scales $F_{\rm var} \sim 2$ per cent (from the 'good' OM observations).

The excess variance in 4 of the 15 *XMM–Newton* OM observations is found to be considerably greater than the remaining 11. The 'poor' 11 observations show that there is a 'floor' to the excess variance that is not accounted for in the errors. In the 'poor' observations any intrinsic source variations are masked by the errors, and inclusion of these observations will weaken the detection of any correlated emission. Although 4 out of the 15 observations are a relatively small subset, we find the variability statistics of the 4 'good' observations clearly very different from the remaining 11 'poor'. The similarity in the overall shape of the CCF for the four 'good' observations is hard to explain as arising by chance if they were all representative of uncorrelated emission. Nevertheless, the interpretation of the time lag is still treated with some caution.

Analysis of the UV PSD reveals a red-noise light curve with a power-law slope of index $\alpha = 2.62 \pm 0.48$ for the four 'good' OM observations. We searched for correlations between the two bands on time-scales up to ∼40 ks, treating all the *XMM–Newton* and the four 'good' observations separately. The CCF for the four good observations revealed a significant peak of ∼0.5 at a lag of ∼3 ks. Using all 15 *XMM–Newton* observations the CCF revealed a weak correlation (∼0.1) with a peak at ∼3 ks. The cross-spectrum showed the lowest five frequency bins to have a low mean coherence of ∼0.2 and a mean phase lag of ∼3 ks in both cases. Combining the *XMM–Newton* and *Swift* data sets we searched for correlated emission on time-scales up to 40 d and find no significant correlations. The lag significance in the above results was estimated using simulated light curves. A correlation coefficient of $r \sim 0.5$ means the amount of UV variance predictable from the X-ray variance is $r^2 \sim 0.25$. As the coherence is a 'square' quantity, this value is consistent with the ∼0.2 from the coherence.

From an ∼12 yr monitoring campaign on NGC 4051 using ground-based optical photometry, Breedt et al. (2010) estimated the PSD in the frequency range $\sim 10^{-8}$–10^{-3} Hz. In their fig. 4 they fit an unbroken power law to the PSD with $\alpha = 1.4^{+0.6}_{-0.2}$. In the paper Breedt et al. (2010) fitted a single-bend power-law model to the PSD, as is observed for X-rays (e.g. McHardy et al. 2004; Vaughan et al. 2011). Whilst they do not rule out the single-bend model, they find that their data are more consistent with an unbroken power law. Their fig 5 shows the acceptance probabilities for the single-bend model as a function of the high-frequency slope $\alpha_{\rm H}$ and bend frequency $\nu_{\rm B}$. Taking our value of $\alpha \approx 2.5$ as the high-frequency slope this would give a break frequency of $\nu_{\rm B} \approx 10^{-6.5}$ Hz. Our PSD is better constrained in the high-frequency range ($\sim 10^{-5}$–10^{-3} Hz) and so the slope value $\alpha = 2.62 \pm 0.48$ is consistent with their single-bend model.

In a sample of four AGN using *Kepler data*, Mushotzky et al. (2011) estimated power spectral slopes (assuming a single power-law model) of ∼2.6–3.3 to the optical PSD in the $\sim 10^{-6.5}$–$10^{-3.5}$ Hz range. They do not attempt to fit a single-bend power-law model to their PSDs, but the break frequency for the larger black hole masses ($\sim 10^7\,{\rm M}_\odot$) in their sample would likely occur at lower frequencies than they estimate in the PSD.

The X-ray PSD in Fig. 5 shows orders of magnitude more variability power than the UV. This is consistent with what is seen in optical PSDs, where the high-frequency power is much less than in the X-rays, although the amplitudes can be similar (or even greater) at low frequencies (e.g, NGC 3783, Arévalo et al. 2009). A study with simultaneous UV and X-ray coverage on longer time-scales is still lacking. A bend can be seen in the X-ray PSD at $\sim 2 \times 10^{-4}$ Hz (Vaughan et al. 2011). If a break were present in the UV PSD, it would be seen to occur at much lower frequencies than that of the X-ray due to the radius of UV emission being much greater than that of the X-rays.

To assess whether the observed X-ray variations are significant enough to produce the variations seen in the UV band, we compare the root-mean-square luminosity variations in both bands. If the luminosity variations in the UV band are greater than the luminosity variations in the 0.2–10.0 keV band, then this would in effect rule out the 0.2–10.0 keV X-ray variations being the dominant cause of variations in the UV band. The values in Table 3 show that the integrated X-ray luminosity is greater than in the UVW1 band, and the X-ray luminosity variations are a factor of ∼10 greater. It is worth noting here that the UVW1 filter is very narrow compared to the X-rays. The X-ray band covers a factor of ∼50 in wavelength, and the UVW1 band covers only a factor of 1.3. This largely explains the apparently low luminosity in the UWV1 compared to X-rays. The

Table 3. UV and X-ray rms luminosity for the 15 *XMM–Newton* observations.

Band	$\bar{L}$ (10^{41} erg s^{-1})	$L_{\rm rms}$ (10^{41} erg s^{-1})
UVW1	3.4	0.3
0.2–10 keV X-ray	7.3	3.9
1–1.2 keV X-ray	0.3	0.2
5–6 keV X-ray	0.5	0.2

[2] http://ledas-www.star.le.ac.uk/pimms/w3p/w3pimms.html

ratio of the full width at half-maximum to the central wavelength of the UVW1 filter is 620 Å/2910 Å ≈ 0.2. Table 3 gives the rms luminosity for X-ray bands of comparable fractional energy range to the UVW1 filter. The rms luminosity in the narrower X-ray bands is now comparable to that of the UV band, albeit with lower mean luminosity. This shows that, in principle, the X-ray variations could drive variations in the UV band.

Given the published black hole mass ($M_{\rm BH} \approx 1.7 \pm 0.5 \times 10^6\,{\rm M}_\odot$; Denney et al. 2009) it is possible to make predicted lag estimates for each reprocessing scenarios based on standard disc equations to find the distance of the UV emitting. In the Compton up-scattering scenario the lags can be expected to be seen in the ∼1.5–7 ks range for assumed accretion rate as a fraction of Eddington of 0.01–0.1. In the thermal reprocessing scenario the time lags depend on the luminosity of the X-ray band and are expected to be ∼7 ks. The direction and magnitude of our lag from the 'good' data are consistent with the thermal reprocessing scenario. Although the expected time delay of ∼7 ks is predicted from the toy model, the model assumes that the disc is heated solely from the incident X-rays, which are themselves coming from a radius $r = 0$. Both these assumptions are not likely to be true for a real AGN. An extended corona will increase $R_{\rm X}$ and a viscously heated disc will decrease $R_{\rm UV}$ and hence the light travel time between the two emitting regions. In the propagating accretion rate fluctuation model (Arévalo & Uttley 2006) the time-scale of mass flow is dictated by the viscous time-scale. This is dependent on the assumed viscosity parameter and scale height of the geometrically thin, optically thick accretion disc (Czerny 2006). We estimate this to be in the region of ∼weeks–years.

Given the quality of the UV data in the four 'good' observations, a lag in the region of ∼1.5–7 ks would have manifested itself in the cross-correlation analysis. If the lag estimate from the four 'good' observations is to be believed, then crudely speaking ∼25 per cent of the UV and X-ray variance are correlated on time-scales of days. This is consistent with the Breedt et al. (2010) result, where an optical–X-ray correlation of ∼30 per cent is reported on time-scales of ∼weeks.

ACKNOWLEDGMENTS

WNA acknowledges support from an STFC studentship. This research has made use of NASA's Astrophysics Data System Bibliographic Services, and the NASA/IPAC Extragalactic Data base (NED) which is operated by the Jet Propulsion Laboratory, California Institute of Technology, under contract with the National Aeronautics and Space Administration. This paper is based on observations obtained with *XMM–Newton*, an ESA science mission with instruments and contributions directly funded by ESA Member States and the USA (NASA).

REFERENCES

Arévalo P., Uttley P., 2006, MNRAS, 367, 801
Arévalo P., Uttley P., Kaspi S., Breedt E., Lira P., McHardy I. M., 2008, MNRAS, 389, 1479
Arévalo P., Uttley P., Lira P., Breedt E., McHardy I. M., Churazov E., 2009, MNRAS, 397, 2004
Arnaud K. A., 1996, in Jacoby G. H., Barnes J., eds, ASP Conf. Ser. Vol. 101, XSPEC: The First Ten Years. Astron. Soc. Pac., San Francisco, p. 17
Bendat J., Piersol A., 1986, Random Data: Analysis and Measurement Procedures. A Wiley-Interscience publication, Wiley, New York
Box G. E. P., Jenkins G. M., eds, 1976, Time Series Analysis: Forecasting and Control, Holden-Day, San Francisco
Breedt E. et al., 2009, MNRAS, 394, 427
Breedt E. et al., 2010, MNRAS, 403, 605
Burrows D. N. The Swift XRT Team, 2004, Bull. Am. Astron. Soc., 36, 929
Cackett E. M., Horne K., Winkler H., 2007, MNRAS, 380, 669
Cameron D. T., McHardy I., Dwelly T., Breedt E., Uttley P., Lira P., Arevalo P., 2012, MNRAS, 422, 902
Collin S., 2001, in Aretxaga I., Kunth D., Mújica R., eds, Advanced Lectures on the Starburst-AGN Accretion and Emission Processes in AGN, EDP Sciences, Paris, p. 167
Czerny B., 2006, in Gaskell C. M., McHardy I. M., Peterson B. M., Sergeev S. G., eds, ASP Conf. Ser. Vol. 360, The Role of the Accretion Disk in AGN Variability. Astron. Soc. Pac., San Francisco, p. 265
Denney K. D., Watson L. C., Peterson B. M., 2009, ApJ, 702, 1353
Done C., Ward M. J., Fabian A. C., Kunieda H., Tsuruta S., Lawrence A., Smith M. G., Wamsteker W., 1990, MNRAS, 243, 713
Edelson R. A., Krolik J. H., 1988, ApJ, 333, 646
Evans P. A., Beardmore A. P., Page K. L., 2009, MNRAS, 397, 1177
Fabian A. C. et al., 2009, Nat, 459, 540
Fougere P. F., 1985, J. Geophys. Res., 90, 4355
Gehrels N., Chincarini G., Giommi P., Mason K. O., 2004, ApJ, 611, 1005
Guilbert P. W., Rees M. J., 1988, MNRAS, 233, 475
Haardt F., Maraschi L., 1991, ApJ, 380, L51
Mason K. O. et al., 2001, A&A, 365, L36
Mason K. O. et al., 2002, ApJ, 580, L117
McHardy I. M., Papadakis I. E., Uttley P., Page M. J., Mason K. O., 2004, MNRAS, 348, 783
Miyamoto S., Kitamoto S., 1989, Nat, 342, 773
Mushotzky R. F., Done C., Pounds K. A., 1993, ARA&A, 31, 717
Mushotzky R. F., Edelson R., Baumgartner W., Gandhi P., 2011, ApJ, 743, L12
Nandra K., Clavel J., Edelson R. A., George I. M., Malkan M. A., Mushotzky R. F., Peterson B. M., Turner T. J., 1998, ApJ, 505, 594
Nandra K., Le T., George I. M., Edelson R. A., Mushotzky R. F., Peterson B. M., Turner T. J., 2000, ApJ, 544, 734
Nowak M. A., Vaughan B. A., Wilms J., Dove J. B., Begelman M. C., 1999, ApJ, 510, 874
Peterson B. M. et al., 2000, ApJ, 542, 161
Poole T. S., Breeveld A. A., Page M. J., Landsman W., 2008, MNRAS, 383, 627
Priestley M., 1981, Spectral Analysis and Time Series. Vol. 1: Probability and Mathematical Statistics. Academic Press, New York
Roming P. W. A., Kennedy T. E., Mason K. O., 2005, Space Sci. Rev., 120, 95
Russell D. G., 2002, ApJ, 565, 681
Shang Z. et al., 2011, ApJS, 196, 2
Shemmer O., Uttley P., Netzer H., McHardy I. M., 2003, MNRAS, 343, 1341
Smith R., Vaughan S., 2007, MNRAS, 375, 1479
Strüder L., Briel U., Dennerl K., Hartmann R., 2001, A&A, 365, L18
Timmer J., König M., 1995, A&A, 300, 707
Turner M. J. L., Abbey A., Arnaud M., Balasini M., Barbera M., Belsole E., Bennie P. J., Bernard J. P., 2001, A&A, 365, L27
Uttley P., 2006, in Gaskell C. M., McHardy I. M., Peterson B. M., Sergeev S. G., eds, ASP Conf. Ser. Vol. 360, The Relationship Between Optical and X-ray Variability in Seyfert Galaxies. Astron. Soc. Pac., San Francisco, p. 101
Uttley P., McHardy I. M., Papadakis I. E., 2002, MNRAS, 332, 231
Uttley P., Edelson R., McHardy I. M., Peterson B. M., Markowitz A., 2003, ApJ, 584, L53
Uttley P., McHardy I. M., Vaughan S., 2005, MNRAS, 359, 345
van der Klis M., 1989, in Ögelman H., van den Heuvel E. P. J., eds, Timing Neutron Stars, NATO ASI Series C, Volume 262. Kluwer, Dordrecht, p. 27
Vaughan B. A., Nowak M. A., 1997, ApJ, 474, L43
Vaugahn S., Uttley P., 2007, Proc. SPIE, 6603, 660314
Vaughan S., Edelson R., Warwick R. S., Uttley P., 2003, MNRAS, 345, 1271

Vaughan S., Uttley P., Pounds K. A., Nandra K., Strohmayer T. E., 2011, MNRAS, 413, 2489
Welsh, 1999, PASP, 111, 1347W

APPENDIX A: SIMULATING LIGHT CURVES

The red-noise nature of UV light curves means that individual data points in the light curve are correlated with adjacent points. Confidence intervals were placed on the CCF and cross-spectrum measurements from the 15 *XMM* observations using Monte Carlo simulations of uncorrelated light curves. We used the method of Timmer & König (1995) to simulate 10^4 light curves in each band with length 50 d, the same time resolution as the re-binned data ($\Delta t = 1500$ s) and appropriate PSD shapes. The X-ray PSD was modelled by a bending power law with low-frequency slope -1.1, high-frequency slope -2.0 and break frequency 2×10^{-4} Hz parameters from Vaughan et al. (2011). The observed rms–flux relation (see Uttley, McHardy & Vaughan 2005) was added to the simulated X-ray light curves by computing the exponential function of each point (Uttley et al. 2005; Vaughan & Uttley 2007). The UV PSD was modelled with an unbroken power-law with slope -2.1 (see Section 3). Observational noise was added to each simulated UV and X-ray light curve by drawing a Poisson random deviate with mean equal to the mean count per bin in the real light curves. We then took 15 segments corresponding to the times and length of each real observation from the 50 d simulated light curves. The CCF was computed for each segment before averaging. This results in 10^4 simulations of the averaged CCFs from which we extracted the confidence intervals at each lag. Confidence intervals on the cross-spectrum lag and coherence were computed using the same approach.

Light curves were simulated to put confidence intervals on the DCF using the above procedure, except that the generated light curves were 20 times longer than before (1000 d). The time resolution was 1500 s for *XMM*, 500 s for *Swift* and 500 s for the combined data sets. A 50 d segment was then selected at random from this light curve and points then sampled from this coinciding with times and lengths of the real *XMM* and *Swift* observations.

In order to set an upper limit on coherence we simulated light curves with added variance, i.e. some fraction A of the simulated X-rays was added to the simulated UV. The variances were normalized before the two light curves were added. We simulated 10^4 light curves in each band for a range added variance and recorded the mean coherence value for the lowest five Fourier frequencies. The bias in coherence (Bendat & Piersol 1986, section 9.2.3) is given by $B[\gamma^2] = 1/n(1 - \gamma^2)^2$ where γ^2 is the coherence and n is the number of segments going into the cross-spectrum (15 in our simulations). When the coherence is low the bias dominates and acts to shift up the observed coherence value and must be subtracted from the computed value. The distribution in coherence values for each A were then compared to our observed coherence value $\gamma^2_{\rm obs}$. The mean coherence value for the distribution of coherences where 90 per cent of the values fall above $\gamma^2_{\rm obs}$ is taken as the upper limit.

This paper has been typeset from a TEX/LATEX file prepared by the author.